Sandwich-Lithiation and Longitudinal Crack in Amorphous Silicon Coated on Carbon Nanofibers

Jiang Wei Wang,[†,¶] Xiao Hua Liu,[‡,¶,*] Kejie Zhao,[§] Andrew Palmer,[⊥] Erin Patten,[⊥] David Burton,[⊥] Scott X. Mao,[†] Zhigang Suo,[§] and Jian Yu Huang[‡,*]

[†]Department of Mechanical Engineering and Materials Science, University of Pittsburgh, Pittsburgh, Pennsylvania 15261, United States, [‡]Center for Integrated Nanotechnologies, Sandia National Laboratories, Albuquerque, New Mexico 87185, United States, [§]School of Engineering and Applied Sciences, Harvard University, Cambridge, Massachusetts 02138, United States, and [⊥]Applied Sciences, Inc., Cedarville, Ohio 45314, United States. [¶]These authors contributed equally to this work.

ABSTRACT

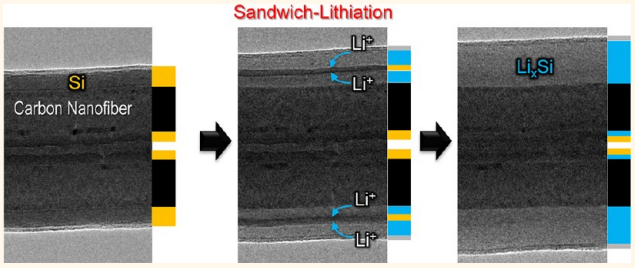

Silicon—carbon nanofibers coaxial sponge, with strong mechanical integrity and improved electronic conductivity, is a promising anode structure to apply into commercial high-capacity lithium ion batteries. We characterized the electrochemical and mechanical behaviors of amorphous silicon-coated carbon nanofibers (*a*-Si/CNFs) with *in situ* transmission electron microscopy (TEM). It was found that lithiation of the *a*-Si coating layer occurred from the surface and the *a*-Si/CNF interface concurrently, and propagated toward the center of the *a*-Si layer. Such a process leads to a sandwiched Li_xSi/Si/Li_xSi structure, indicating fast Li transport through the *a*-Si/CNF interface. Nanocracks and sponge-like structures developed in the *a*-Si layer during the lithiation-delithiation cycles. Lithiation of the *a*-Si layer sealed in the hollow CNF was also observed, but at a much lower speed than the counterpart of the *a*-Si layer coated on the CNF surface. An analytical solution of the stress field was formulated based on the continuum theory of finite deformation, explaining the experimental observation of longitudinal crack formation and general mechanical degradation mechanism in *a*-Si/CNF electrode.

KEYWORDS: amorphous silicon · carbon nanofiber · interface · crack · lithium ion battery · *in situ* TEM

Nanostructuring and compositing are currently being pursued as important strategies to fabricate high performance electrodes for lithium ion batteries (LIBs).[1,2] For the former, it has been demonstrated that active materials with sufficiently small sizes are able to avert lithiation-induced stress accumulation and fracture,[3−8] and to allow fast charging and discharging.[9,10] For the latter, the overall performance of an electrode, in terms of higher energy density, power density, and cyclability, could be enhanced by rationally tailoring the mixture of the active materials and additives such as a conducting matrix or structural buffer.[11−15]

Amorphous silicon coated carbon nanofiber (*a*-Si/CNF) composite nanostructures have several advantages as an anode material for LIBs. First, a combination between the high gravimetric capacity of Si and excellent stability of CNF promises to boost overall performance.[11,13,16−19] Si has the highest theoretical capacity (4200 mAh/g for $Li_{22}Si_5$ at high temperatures[20] or 3579 mAh/g for $Li_{15}Si_4$ at room temperature[21−24]), which is nearly ten times higher than that of graphite (372 mAh/g, LiC_6). However, Si undergoes ~300% volumetric expansion during lithiation, often leading to fracture,[3,24,25] pulverization, and rapid capacity-fading of the Si-based electrodes.[13] In contrast, carbonaceous anodes exhibit great cyclability with less than 10% volumetric changes upon lithium insertion and extraction. Combining Si and CNF provides tunable capacity, electrical, and mechanical properties. Second, crystalline Si undergoes anisotropic swelling during lithiation, namely fast lithiation along ⟨110⟩ and slow lithiation along ⟨111⟩ crystal orientations.[24−27] Such anisotropic expansion can be avoided by using *a*-Si.[28] Third, the mass loading can be feasibly increased by repeated stacking, while the thinness of the *a*-Si and the mechanically robustness of the CNF scaffold are maintained for high rate performance and cyclability. Takamura *et al.* demonstrated high capacity up to 2000 mAh/g and high rate performance up to 30C (*i.e.*, full lithiation in 2 min) of *a*-Si deposited on a nickel substrate; however, the *a*-Si film was only 50-nm thick on the planar substrate

* Address correspondence to lxhua99@gmail.com, jyhuang8@yahoo.com.

Received for review July 31, 2012 and accepted September 17, 2012.

Published online September 17, 2012
10.1021/nn3034343

and could not go thicker.[9] On the other hand, Hu *et al*. demonstrated increasing the areal capacity by using stacked *a*-Si/CNFs, that is, the three-dimensional (3D) sponge-like structures.[16] Since a single material is unlikely to meet all the requirements at the same time, nanostructured composite materials will be the preferred method to achieve high performance.

Despite constant efforts to develop Si/C composite electrode materials in all forms,[11,17,29,30] a fundamental understanding of the lithiation and failure mechanisms is still lacking. Recently, Wang *et al*. reported the first *in situ* transmission electron microscopy (TEM) investigation of the microstructural evolution of individual *a*-Si/CNF structures in a nanobattery with an ionic liquid electrolyte, which showed the structural evolution and phase transformation in the composite nanomaterial.[28] It was suggested that the *a*-Si layer on the CNF was lithiated to an amorphous Li−Si alloy (*a*-Li_xSi) in a sequential manner, that is, a lithiation front propagated along the Li^+ diffusion direction and converted *a*-Si into *a*-Li_xSi accompanied by instant swelling, and finally the *a*-Li_xSi was converted to the crystalline $Li_{15}Si_4$ (*c*-$Li_{15}Si_4$) phase.[28] However, because of the electron-beam-induced gelation of the ionic liquid electrolyte, a thick jelled electrolyte layer was formed on the nanowire that prevented observation of fine structural changes.[28] Ghassemi *et al*. reported the *in situ* TEM lithiation tests of *a*-Si nanorods (not composited with carbon) and claimed formation of the $Li_{22}Si_5$ phase upon full lithiation.[31] Herein, we report an unexpected observation of the sandwich-lithiation mechanism of the *a*-Si/CNF composite, featuring simultaneous lithiation from the *a*-Si surface and the *a*-Si/CNF interface and thus formation of a Li_xSi/Si/Li_xSi sandwiched structure in the coating layer during lithiation. Such observation was made possible by the *in situ* TEM experiments in the solid cell configuration, which utilizes a solid-state electrolyte of Li_2O that does not wet the nanowire surface.[32,33]

RESULTS AND DISCUSSION

Figure 1a shows a schematic illustration of the *in situ* experimental setup with a half-cell configuration. The CNFs were hollow and sometimes filled with porous *a*-Si during the coating process (Figure 1a,b), in which a uniform *a*-Si layer was deposited onto the CNF surface. Figure 1b,c shows the typical morphology change of an *a*-Si/CNF nanowire with a partially filled hollow cavity. Both the surface and inner *a*-Si layers showed obvious swelling, characterized by the increased thickness and decreased pore sizes (Figure 1c), respectively. The thickness of the surface *a*-Si layer increased from ~7 to 25 nm after lithiation, corresponding to about 260% volumetric expansion. The inner diameter of the hollow CNF increased from 112 to 122 nm, probably due to the expansion of the sealed *a*-Si during lithiation. The elliptical pores shrank (marked by the dashed yellow circles in Figure 1b,c) and the thickness of the inner *a*-Si layer increased, indicating lithiation of the *a*-Si sealed in the CNF and lithium transport through the CNF wall. The CNF had a bilayered tubular structure (Supporting Information, Figure S1). The inner layer (~20 nm thick) was aligned graphitic sheets with a dark contrast, and the outer layer (~55 nm thick) was disordered graphitic clusters with a light contrast (Figure S1). During lithiation, the CNF structure showed little change. Figure 1d,e and Supporting Information, movie S1 compare the morphology of another *a*-Si/CNF wire before and after lithiation. There was no *a*-Si filling in the hollow cavity of this particular CNF (Figure 1d), so only swelling of the surface *a*-Si layer was observed (Figure 1e). To improve the electrical contacts between the outer *a*-Si layer and the current collector, a thin layer of amorphous carbon (*a*-C) was coated onto the wire by sputtering a graphite target (Figure 1d). Such an *a*-C layer also showed obvious expansion in thickness from 4.6 to 7.1 nm (Figure 1e), similar to our previous observations in C-coated Si nanowires.[23]

Intriguingly, an unexpected sandwich-lithiation manner was frequently observed in the *in situ* lithiation tests of the a-Si/CNF structures (Figures 2 and 3 and Supporting Information, Figure S2 and movies S2 and S3). Initially, lithiation occurred through the sequential manner (Figure 2a,b), that is, propagating along both the axial and radial directions. This is expected due to the surface transport of Li^+ and its insertion from the *a*-Si surface to the CNF. However, the following lithiation showed different features evidenced by the dark stripe in the *a*-Li_xSi layer in the segment enclosed by the red dotted box in Figure 2c. It appears that lithiation occurred from both the surface and the interface (Figure 2c), which eventually depleted the residual *a*-Si in the middle (Figure 2d). Figure 3 shows the sequential images that clearly revealed the microstructural evolution of the surface *a*-Si layer during lithiation. Initially, the interface between the CNF and the surface *a*-Si layer was merely visible (Figure 3a). A white line of *a*-Li_xSi with a lower average atomic weight appeared at the *a*-Si/CNF interface (Figure 3b), which extended into the *a*-Si layer with continued lithiation (Figure 3c,d). In the meantime, lithiation occurred from the outmost surface and propagated inward. The initial *a*-Si surface layer was converted to a sandwiched structure, with the unreacted Si with a dark contrast in the middle of the top and bottom *a*-Li_xSi layers with a light contrast due to the lower average atomic weight. It is worth noting that longitudinal Li transport or the sequential lithiation manner still exists, since the radial lithiation at the upstream of Li^+ flow was earlier than that at the downstream (Figure 3c,d). Depletion of the sandwiched *a*-Si layer resulted in a moving tail along the axial lithiation direction, and the radial lithiation

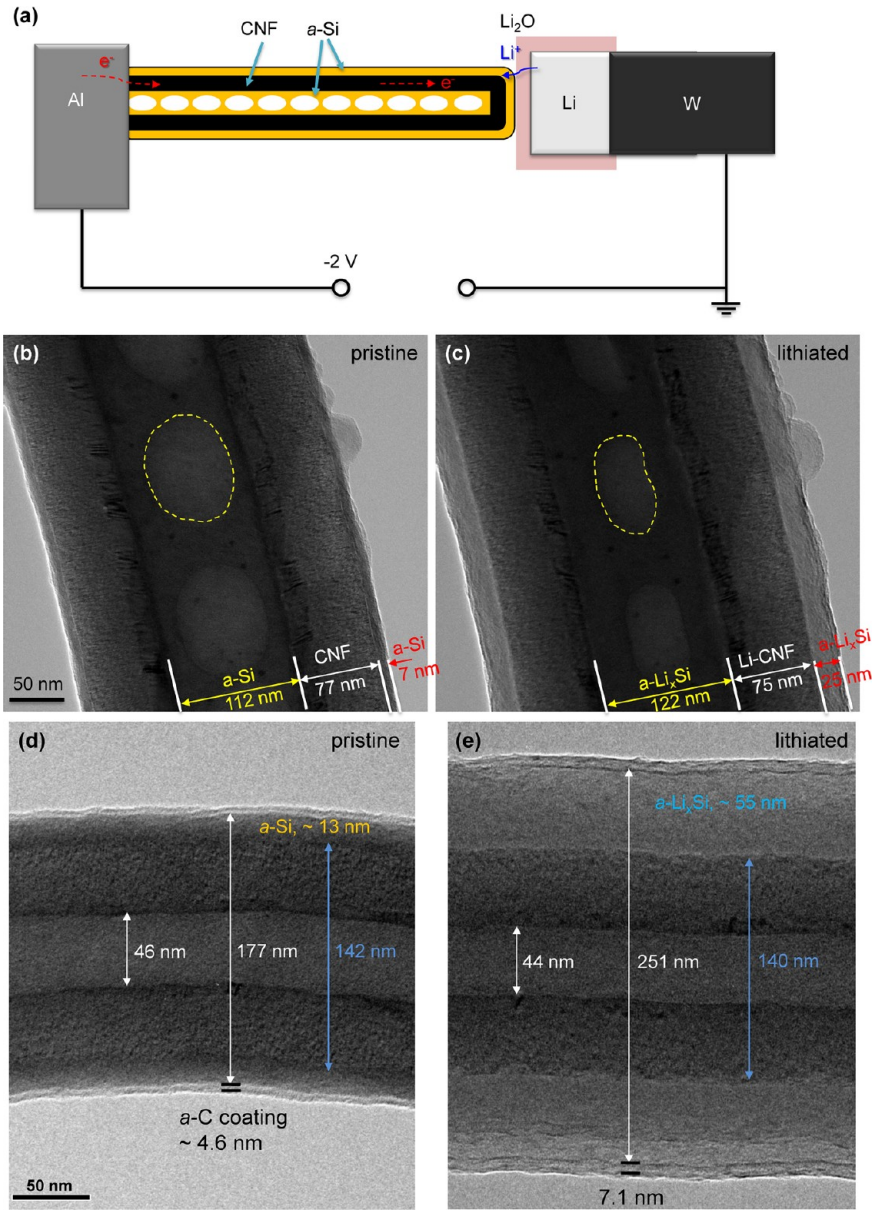

Figure 1. ***In situ*** **experimental setup and typical microstructural changes during lithiation of the amorphous Si on carbon nanofiber (*a*-Si/CNF) anode. (a) Schematic illustration of the half-cell configuration for the *in situ* electrochemical lithiation−delithiation tests inside a TEM. The working electrode is an individual CNF (black) coated with a uniform a-Si layer (yellow). Some CNFs are also partially filled with *a*-Si. A Li metal on a W probe is the counter electrode, and the native Li_2O layer on Li metal serves as a solid-state electrolyte for Li transport. (b,c) Morphology change of a partially filled CNF. The surface coating layer of *a*-Si was thickened from 7 to 25 nm after lithiation, and the porous a-Si in the hollow CNF expanded from 112 to 122 nm, while the thickness of the CNF wall slightly decreased from 77 to 75 nm. The pores in the inner *a*-Si part shrank due to the volume expansion of Si during lithiation (marked by the yellow dashed circles). (d,e) Morphology change of a CNF without Si filling in the hollow tube. The Si coating layers was thickened from ~13 to 55 nm after lithiation, and the CNF structure was almost unchanged during lithiation. The outmost amorphous carbon layer was thickened from 4.6 to 7.1 nm after lithiation, indicating that carbon was also lithiated.**

seemed to be uneven on the circumference because the tail positions were different (marked by the top and bottom arrows in Figure 3e). Finally, the surface *a*-Si layer was completely converted to *a*-Li_xSi (Figure 3f), and the inner *a*-Si inside the CNF was also partially lithiated, as the white lines (*i.e.*, contrast of *a*-Li_xSi, marked by the blue arrows in Figure 3f) appeared at the interfaces between the inner *a*-Si (dark stripes, marked by the yellow bars in Figure 3f) and the CNF.

Our observations revealed some previously unknown features of the fine structural changes in the composite nanowire during lithiation. (1) The *a*-Si/CNF interface also served as the fast Li^+ transport channel. Lithiation at the interface should replace most Si−C bonds into Li−C bonds, and change the interface property. This is consistent with the previously observed fast diffusion of Li on carbonaceous materials such as carbon nanotubes and graphene.[34] According

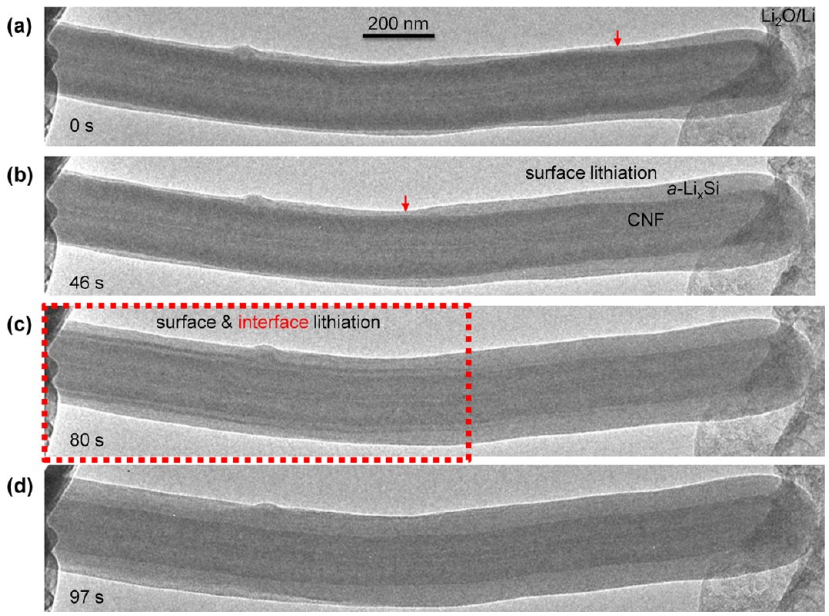

Figure 2. Lithiation of the surface Si coating layer. (a,b) Surface lithiation regime. Initially the lithiation was characterized by a moving reaction front (marked by the red arrows) followed by the swelling segment with a uniform light contrast that indicates the phase transformation from *a*-Si to *a*-Li_xSi with reduced average atomic weight. (c,d) Surface and interface lithiation (or so-called "sandwich-lithiation") regime. At this stage, lithiation occurred from both the *a*-Si surface and the *a*-Si/CNF interface (marked by the red dotted box in panel c). The coating layer became a layered structure of Li_xSi/Si/Li_xSi, showing a unique striped contrast with the dark unreacted Si in the center.

to the radial lithiation speed ratio and thickening of the top and bottom *a*-Li_xSi layers in the sandwich structure, the Li flux through the interface diffusion is about 80% of that through surface diffusion (Figure 3d). The sandwich-lithiation mechanism may have a significant impact on the fracture of the coating layer and stability of the entire composite structure, because the lithiation at the *a*-Si/CNF interface is believed to change the bonding/adhesion of the coating layer to the structural support. (2) Lithiation of the sealed Si in the CNF is possible but relatively slow. Lithium transport through the CNF wall occurs when there is an opening on the CNF wall or the defective CNF wall is permeable to Li^+ ions. In our experiments, lithiation of the inner *a*-Si in the CNF cavity predominantly took place from the *a*-Si/CNF interface (such as the widening white lines in Figure 3f), but the sandwiched structure was not observed for the inner *a*-Si due to the lack of obvious surface lithiation from the inner *a*-Si surface. This may imply that Li transport is possible through the CNF backbone, as evidenced by lithiation of the *a*-Si layers on the two sides of the CNF wall. Further investigations are needed to identify the lithiation mechanism of the sealed Si. Nevertheless, the inner *a*-Si sealed in the hollow CNF can be lithiated (Figures 1c, 3f), although at a relatively slower speed than the outer coating layer. This is consistent with the concept of pocketed Si demonstrated by Hertzberg *et al.*,[35] however, it also suggests that the carbon pocket should not be too thick. The lithiation kinetics is likely rate-controlled by the Li diffusion through *a*-Si/CNF interfaces, while the stable CNF provides excellent mechanical and electrical support to the active materials sealed in it.

Figure 4 and Supporting Information, movie S4 show the typical microstructural evolution during the lithiation−delithiation cycles. In the first few cycles, the coated *a*-Si layer underwent nearly reversible volumetric expansion and shrinkage. However, the uniform *a*-Si coating became roughened and showed longitudinal cracks running parallel to the CNF axis (marked by the red arrows in Figure 4e,f). The cracks typically nucleated during the delithiation process (Figure 4e), and became obvious during the following lithiation process (Figure 4f). The surface roughening and crack nucleation during delithiation are due to the plastic flow of lithiated silicon.[9,16,36,37] Detailed modeling is described in the following section. The electron diffraction patterns indicated that the pristine *a*-Si (Figure 4g) first underwent the phase transformation to form *a*-Li_xSi, which might partially or completely crystallize to the *c*-$Li_{15}Si_4$ phase (Figure 4h).[24,28] The lithiated *a*-Li_xSi or *c*-$Li_{15}Si_4$ phases transformed back to *a*-Si after delithiation (Figure 4i). It should be noted that we did not observe noticeable changes in the diffraction patterns from the CNF, such as the spacing expansion of the basal planes in the graphitic sheets as observed in carbon nanotubes or few-layered graphene,[34,38] indicating a low degree of lithiation in the CNF, which is consistent with the negligible small morphology changes.

Figure 5 shows the longitudinal nanocrack formation in the *a*-Si coating layer after cycling. Reversible

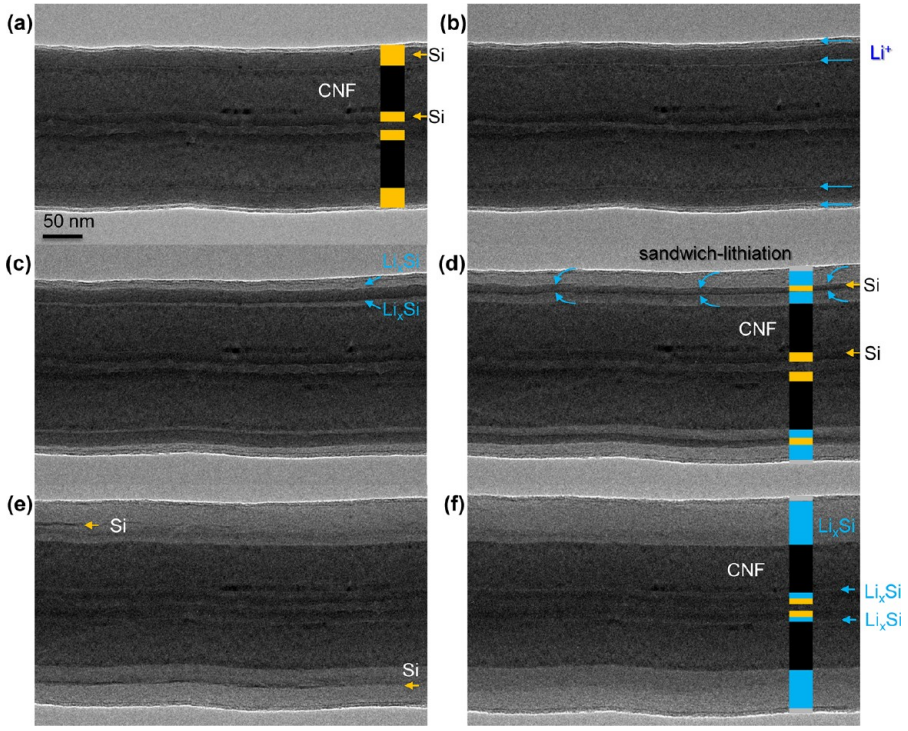

Figure 3. Close view of the sandwich-lithiation manner. (a) Pristine *a*-Si/CNF structure. The superimposed scheme shows the coaxial layers of materials. The yellow arrows mark the positions of the *a*-Si layers on the CNF surface and hollow cavity, respectively. (b–d) Upon lithiation, Li^+ ions diffused from the right to the left, followed by lithiation through the surface and the interface (blue arrows). The unreacted *a*-Si layer was sandwiched in two layers of *a*-Li_xSi (c,d). Note that the layer thicknesses were not uniform along the length, indicating that Li transport/insertion along both axial and radial directions. A scheme of the layered structure is superimposed on the TEM image shown in panel d to illustrate the intermediate structure during lithiation (blue, Li_xSi; yellow, *a*-Si; black, CNF). (e) Depletion of *a*-Si in the surface coating layer. With continued lithiation, the *a*-Si layer was consumed by the top and bottom *a*-Li_xSi layers, resulting in moving tails of the *a*-Si layer (marked by the yellow arrows). The radial lithiation speed varied, evidenced by the different tail positions. (f) Morphology upon completion of lithiation. Some stripes were visible along the axial directions, probably due to the uneven lithiation. A superimposed scheme shows that the surface *a*-Si was fully lithiated to *a*-Li_xSi but the sealed *a*-Si was only partially lithiated (blue bars in the scheme and the white lines at the interfaces in the TEM image).

volumetric changes took place in the lithiation–delithiation cycles (Figure 5a–k), and the lithiated phase could be either amorphous (Figure 5b,d,h) or crystalline (Figure 5f,j).[28] Close examination of the structure after cycling reveals nanocracks (marked by the red arrowheads in Figure 5l) and a sponge-like structure, consistent with the previous results obtained in the liquid-electrolyte-based *in situ* nanobattery[28] or *ex situ* cells.[16] Interestingly, the nanocracks were mostly orientated along the longitudinal directions (*i.e.*, parallel to the CNF's axis). Such longitudinal cracks are due to the tensile stress in the hoop direction, which drives the initial flaws (*i.e.*, preexisting cracks) in the axial orientation to propagate. We note that, to accommodate the large volumetric expansion during lithiation cycles, the lithiated silicon must deform plastically. To illustrate the salient feature of the stress field, we consider that the silicon coating is uniformly lithiated. This is not an unreasonable assumption when the feature size of the silicon shell is small such that the diffusion of lithium is a fast process through silicon. As the lithiation progresses, the lithiated silicon enlarges. Such expansion is constrained by the carbon core. An element in the curved lithiated silicon undergoes tensile stress in the radial direction, and compressive stresses in the hoop and axial directions. Upon subsequent delithiation, the element unloads elastically, and then deforms plastically in compression in the radial direction, while in tension in the hoop and axial directions. This process can cause the initial flaws in the silicon shell to grow, leading to the fracture of the lithiated silicon.[37] It is worth noting that the fracture event does not necessarily lead to immediate failure of the battery, as long as a good bonding is maintained between the lithiated silicon shell and the conductive carbon backbone. Nevertheless, the fatigue fracture associated with the cyclic plastic deformation of silicon could become a major degradation mechanism of such architecture in the cycle life.

We derive the stress field in a silicon–carbon nanofibers coaxial structure using the continuum theory of finite deformation.[39] The geometry is represented in Figure 6a. We represent a material element in the reference configuration by its distance R from the center. At time t, the material element moves to a place at a distance r from the center. The function $r(R, t)$

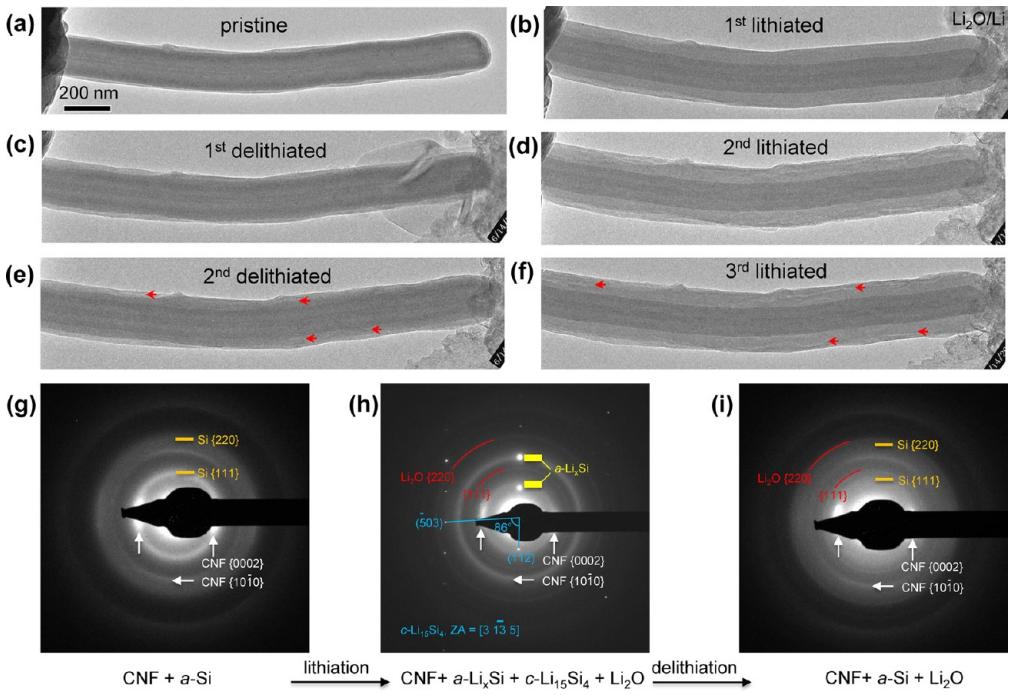

Figure 4. Microstructural changes during the lithiation-delithiation cycles. (a-f) Morphology evolution of an *a*-Si/CNF structure in the first three cycles. The dramatic changes occurred in the surface *a*-Si layer, which swelled and showed a brighter contrast during lithiation. Nanocracks nucleated during the second delithiation process (e) and became more obvious during the third lithiation process. (g−i) Electron diffraction patterns (EDPs) of the pristine (g), lithiated (h), and delithiated structures (i). Amorphous Li_xSi or crystalline $Li_{15}Si_4$ phases were formed after lithiation, which were converted to *a*-Si after Li extraction.

specifies the deformation kinematics. It is noted that the elastic stiffness of CNF is around 10 times that of the lithiated silicon;[40,41] the deformation of rigid CNFs is neglected. Because of the mechanical constraint imposed by the CNFs in the axial direction, the lithiated silicon is assumed to deform under the plane-strain conditions. To focus on the main ideas, we neglect the elasticity of the lithiated silicon; we model the lithiated silicon as a rigid-plastic material.[42] Consequently, the expansion of lithiated silicon is entirely due to the lithiation. Consider the shell of the lithiated silicon between the radii A and r. This shell is lithiated from the shell of pristine silicon between the radii A and R. We assume that lithium is injected slowly and has sufficient time to diffuse through silicon. The ratio of the volume of the lithiated shell over the volume of pristine silicon, β, is taken to be homogeneous and evolves in time. Thus,

$$r^2 - A^2 = \beta(R^2 - A^2) \tag{1}$$

This equation gives the function $r(R, t)$ once the function $\beta(t)$ is given. That is, $\beta(t)$ fully specifies the kinematics of the silicon shell, $r = (A^2 + \beta(R^2 - A^2))^{1/2}$. The stretches can be calculated as

$$\lambda_r = \frac{\partial r}{\partial R} = \frac{R\beta}{r}, \quad \lambda_\theta = \frac{r}{R}, \quad \lambda_z = 1 \tag{2}$$

We decompose the stretches by writing $\lambda_r = \lambda_r^p\beta^{1/3}$, $\lambda_\theta = \lambda_\theta^p\beta^{1/3}$, $\lambda_z = \lambda_z^p\beta^{1/3}$, where β represents the volume change due to the insertion of lithium, and the plastic stretch λ^p represents the shape change during lithiation. The volume change β has been assumed to be isotropic for amorphous silicon. We can calculate the strain components from the stretches,

$$\varepsilon_r = \log\lambda_r, \quad \varepsilon_\theta = \log\lambda_\theta, \quad \varepsilon_z = \log\lambda_z \tag{3}$$

To calculate the stress field, one has to consider the incremental plastic deformation with respect to time. Given eq 2 and 3, we obtain that

$$\begin{aligned}
\delta\varepsilon_r^p &= \delta\log\lambda_r - \frac{1}{3}\delta\log\beta = \left(\frac{1}{6} + \frac{1}{2}\frac{A^2}{r^2}\right)\frac{\delta\beta}{\beta} \\
\delta\varepsilon_\theta^p &= \delta\log\lambda_\theta - \frac{1}{3}\delta\log\beta = \left(\frac{1}{6} - \frac{1}{2}\frac{A^2}{r^2}\right)\frac{\delta\beta}{\beta} \\
\delta\varepsilon_z^p &= \delta\log\lambda_z - \frac{1}{3}\delta\log\beta = -\frac{1}{3}\frac{\delta\beta}{\beta}
\end{aligned} \tag{4}$$

The equivalent plastic strain increment is

$$\delta\varepsilon_{eq}^p = \sqrt{\frac{2}{3}\delta\varepsilon_{ij}^p\delta\varepsilon_{ij}^p} = \frac{\delta\beta}{\beta}\sqrt{\frac{1}{9} + \frac{1}{3}\frac{A^4}{r^4}} \tag{5}$$

We adopt the flow rule

$$s_{ij} = \frac{2}{3}\frac{\sigma_Y}{\delta\varepsilon_{eq}^p}\delta\varepsilon_{ij}^p \tag{6}$$

where s_{ij} is the deviatoric stress, defined as $s_{ij} = \sigma_{ij} - (1/3)\sigma_{ii}\delta_{ij}$, where δ_{ij} is the Kronecker delta, and

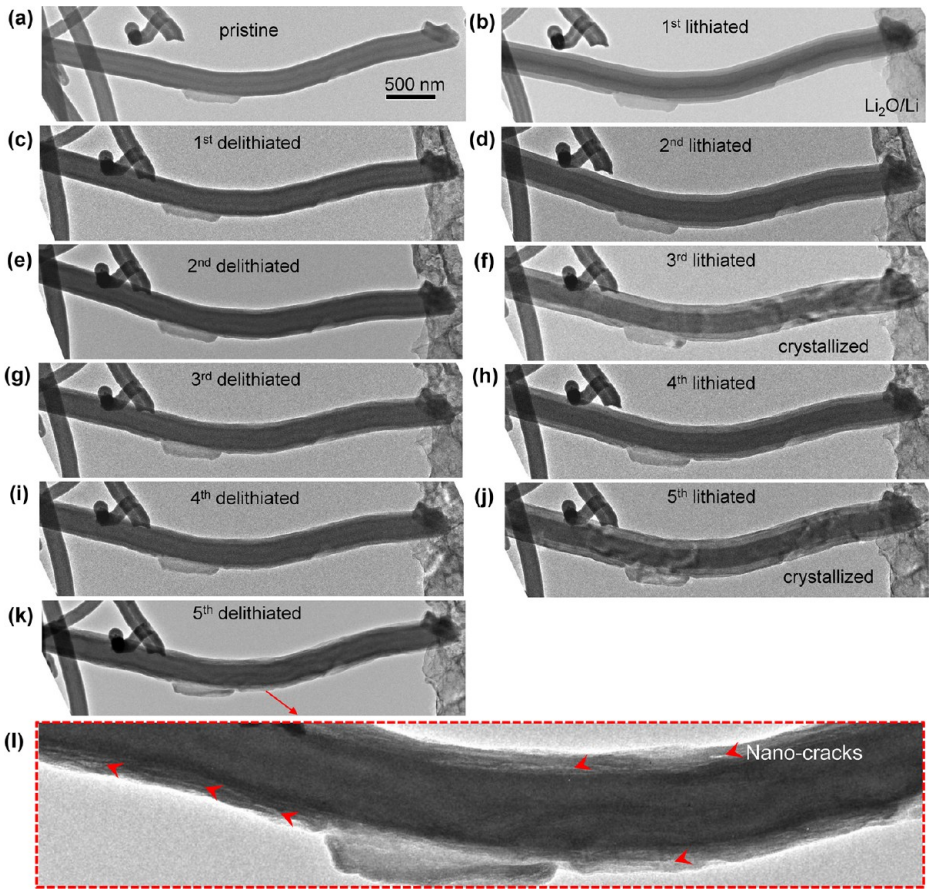

Figure 5. Crack formation after cycling. (a-k) Morphology evolution in the first five lithiation-delithiation cycles. (l) Zoomed-in image of the structure after the fifth delithiation process. The surface coating layer became rough with many nanocracks and sponge-like morphology.

σ_Y the yield strength of lithiated silicon. Therefore,

$$s_r = \frac{\sigma_Y}{\sqrt{\frac{1}{9}+\frac{1}{3}\frac{A^4}{r^4}}}\left(\frac{1}{9}+\frac{1}{3}\frac{A^2}{r^2}\right)$$

$$s_\theta = \frac{\sigma_Y}{\sqrt{\frac{1}{9}+\frac{1}{3}\frac{A^4}{r^4}}}\left(\frac{1}{9}-\frac{1}{3}\frac{A^2}{r^2}\right) \quad (7)$$

$$s_z = -\frac{2}{9}\frac{\sigma_Y}{\sqrt{\frac{1}{9}+\frac{1}{3}\frac{A^4}{r^4}}}$$

and

$$\sigma_r - \sigma_\theta = s_r - s_\theta = \frac{2\sigma_Y}{\sqrt{r^4/A^4+3}} \quad (8)$$

where σ_r, σ_θ, and σ_z represent the radial, hoop, and axial stresses, respectively. Consider the force balance of a material element in lithiated silicon

$$\frac{\partial\sigma_r}{\partial r}+\frac{\sigma_r-\sigma_\theta}{r}=0 \quad (9)$$

the radial stress can be obtained by integrating eq 9, it gives

$$\sigma_r = -\frac{\sqrt{3}}{3}\sigma_Y \log\frac{\sqrt{r^4+3A^4}-\sqrt{3}A^2}{r^2}+D, \quad A\le r\le b \quad (10)$$

The integration constant D is determined by the traction-free boundary condition, $\sigma_r(b, t) = 0$, such that

$$\sigma_r = -\frac{\sqrt{3}}{3}\sigma_Y\left(2\log\frac{b}{r}+\log\frac{\sqrt{r^4+3A^4}-\sqrt{3}A^2}{\sqrt{b^4+3A^4}-\sqrt{3}A^2}\right), \quad A\le r\le b \quad (11)$$

The stresses along hoop and axial directions are obtained by eq 7 and 8,

$$\sigma_\theta = -\frac{\sqrt{3}}{3}\sigma_Y\left(2\log\frac{b}{r}+\log\frac{\sqrt{r^4+3A^4}-\sqrt{3}A^2}{\sqrt{b^4+3A^4}-\sqrt{3}A^2}\right)-\frac{2\sigma_Y}{\sqrt{r^4/A^4+3}}$$

$$\sigma_z = -\frac{\sqrt{3}}{3}\sigma_Y\left(2\log\frac{b}{r}+\log\frac{\sqrt{r^4+3A^4}-\sqrt{3}A^2}{\sqrt{b^4+3A^4}-\sqrt{3}A^2}\right) \quad (12)$$

$$-\sigma_Y\left(\frac{1}{\sqrt{r^4/A^4+3}}+\frac{1}{\sqrt{3A^4/r^4+1}}\right)$$

Note that the stresses along the hoop and axial directions are compressive during lithiation. During

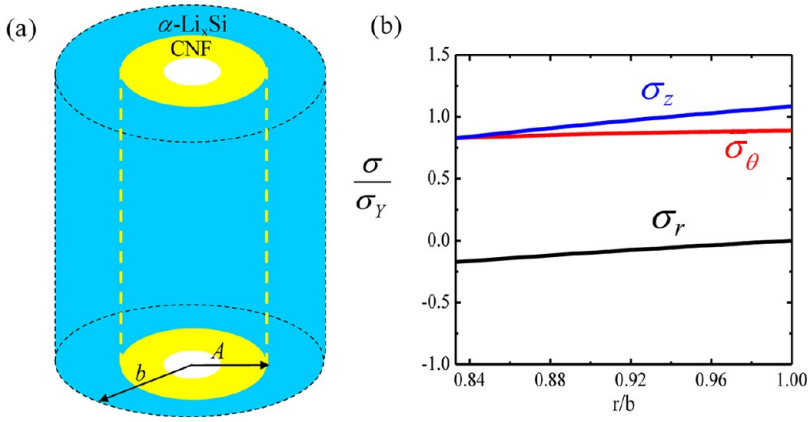

Figure 6. (a) Schematic illustration of an *a*-Si/CNF anode. The radius of carbon core is *A*. Lithiation of the CNF is neglected. During lithiation (delithiation) of the *a*-Si shell, the radius of Si expands to be *b*. (b) Distribution of radial, hoop, and axial stresses (σ_r, σ_θ, σ_z) after delithiation. The stresses are scaled with the yield strength of lithiated silicon σ_Y. Experimental values are taken in the calculations, A = 70 nm, b = 84 nm.

delithiation, however, theses stresses become tensile, and can be calculated by taking the same approach,

$$\sigma_r = \frac{\sqrt{3}}{3}\sigma_Y\left(2\log\frac{b}{r}+\log\frac{\sqrt{r^4+3A^4}-\sqrt{3}A^2}{\sqrt{b^4+3A^4}-\sqrt{3}A^2}\right)$$

$$\sigma_\theta = \frac{\sqrt{3}}{3}\sigma_Y\left(2\log\frac{b}{r}+\log\frac{\sqrt{r^4+3A^4}-\sqrt{3}A^2}{\sqrt{b^4+3A^4}-\sqrt{3}A^2}\right)+\frac{2\sigma_Y}{\sqrt{r^4/A^4+3}}$$

$$\sigma_z = \frac{\sqrt{3}}{3}\sigma_Y\left(2\log\frac{b}{r}+\log\frac{\sqrt{r^4+3A^4}-\sqrt{3}A^2}{\sqrt{b^4+3A^4}-\sqrt{3}A^2}\right) + \sigma_Y\left(\frac{1}{\sqrt{r^4/A^4+3}}+\frac{1}{\sqrt{1+3A^4/r^4}}\right) \quad (13)$$

We plot the stress field after delithiation of the silicon shell, Figure 6b. Experimental values are taken in the calculations, A = 70 nm, b = 84 nm. As aforementioned, the tensile stress in the hoop direction acts as the driving force for the cracks in the longitude directions. A representative value of the yield strength is σ_Y = 1.5 GPa.[38] A representative flaw size is taken to be a fraction of the thickness of the lithiated silicon shell, c = 55 nm. The estimated stress intensity factor is $K = \sigma(\pi c)^{1/2}$ = 0.62 MPa$\sqrt{\text{m}}$. This value may be compared with the fracture toughness $K_c = (\gamma E)^{1/2}$ = 1.09 MPa$\sqrt{\text{m}}$, where γ represents the surface energy, with a typical value ~1 J/m^2, and E Young's modulus of the lithiated silicon ~12 GPa as measured in *ex-situ* indentation experiments.[42] Note that the magnitude of the axial stress is slightly larger than that of the hoop stress, but the observed crack is along the axial direction. This difference between the experimental observation and theoretical prediction is unresolved at this writing.

Does the sandwich lithiation mechanism operate for the *a*-Si/CNF composite anode immersed in a liquid electrolyte in real batteries? Certainly this is an important question to ask, but unfortunately there is no answer yet. This is under investigation despite of the obvious experimental challenges including electron-beam induced damage to organic electrolytes.

CONCLUSION

The electrochemical lithiation and corresponding microstructural evolution of the *a*-Si/CNF composite nanowires were studied with *in situ* TEM in a half-cell configuration. A sandwich-lithiation mechanism was discovered for the first time, revealing fast Li diffusion through the *a*-Si/CNF interface. Lithiation occurred from both the top and bottom surfaces of the *a*-Si layer and propagated through the thickness. Lithiation of the *a*-Si deposited inside the hollow CNF was also observed. Nanocracks and sponge-like structures were formed after lithiation cycles. Fracture of the shell is attributed to the cyclic plastic deformation of the lithiated silicon. An analytical solution of the stress field is obtained based on the continuum theory of finite deformation. Our observations provide an important insight into the electrochemical reactions and failure mechanism of the Si/C composite materials for lithium ion batteries.

EXPERIMENTAL DETAILS

The *a*-Si/CNF samples were prepared by coating *a*-Si onto CNFs with chemical vapor deposition (CVD) method (Applied Sciences Inc.).[28] The thickness of the surface *a*-Si coating layer can be controllably varied. The working electrode was formed by attaching *a*-Si/CNF composite nanowires to an aluminum (Al) rod with conductive silver epoxy. To enhance the electrical transport between the composite nanowires and the Al rod, a thin layer of carbon was coated by sputtering a graphite target. Fresh Li metal was loaded onto a tungsten (W) rod in a glovebox filled with helium (H_2O and O_2 concentration below 1 ppm) and served as the counter electrode and Li source. The two electrodes were mounted onto a Nanofactory TEM-scanning tunneling

microscopy (STM) holder. A native Li_2O layer was formed on the Li metal during the transfer of the holder from the glovebox to the TEM column and served as the solid-state electrolyte.[24,43] Inside the TEM, a piezo-positioner was used to drive the Li_2O/Li terminal toward the *a*-Si/CNF-Al terminal. Once contact was established, a negative bias (such as −2 V) was applied to the *a*-Si/CNF electrode to initiate the lithiation process.

Conflict of Interest: The authors declare no competing financial interest.

Acknowledgment. Portions of this work were supported by a Laboratory Directed Research and Development (LDRD) project at Sandia National Laboratories (SNL) and partly by Nanostructures for Electrical Energy Storage (NEES), an Energy Frontier Research Center (EFRC) funded by the U.S. Department of Energy, Office of Science, Office of Basic Energy Sciences under Award Number DESC0001160. The LDRD supported the development and fabrication of platforms. The NEES center supported the development of TEM techniques. The Sandia-Los Alamos Center for Integrated Nanotechnologies (CINT) supported the TEM capability. Sandia National Laboratories is a multiprogram laboratory managed and operated by Sandia Corporation, a wholly owned subsidiary of Lockheed Martin Company, for the U.S. Department of Energy's National Nuclear Security Administration under Contract DE-AC04-94AL85000. K.Z. and Z.S. acknowledge the support by the National Science Foundation through a grant on lithium-ion batteries (CMMI-1031161). We thank David Burton from Applied Sciences Inc. for providing us the *a*-Si/CNF samples which were produced under OSD SBIR Contract FA8650-10-C-2041 and Army SBIR Contract W56HZV-11-C-0193.

Supporting Information Available: Supporting figures showing the structure of the CNF, lithiation from the interface in another *a*-Si/CNF nanowire; movies showing the sandwich lithiation mechanism of the *a*-Si/CNF nanowires and morphology evolution during the lithiation−delithiation cycles. This material is available free of charge *via* the Internet at http://pubs.acs.org.

REFERENCES AND NOTES

1. Arico, A. S.; Bruce, P.; Scrosati, B.; Tarascon, J. M.; Van Schalkwijk, W. Nanostructured Materials for Advanced Energy Conversion and Storage Devices. *Nat. Mater.* **2005**, *4*, 366–377.
2. Tarascon, J.-M. Key Challenges in Future Li-Battery Research. *Phil Trans. R. Soc. A* **2010**, *368*, 3227–3241.
3. Liu, X. H.; Zhong, L.; Huang, S.; Mao, S. X.; Zhu, T.; Huang, J. Y. Size-Dependent Fracture of Silicon Nanoparticles During Lithiation. *ACS Nano* **2012**, *6*, 1522–1531.
4. Chan, C. K.; Peng, H. L.; Liu, G.; McIlwrath, K.; Zhang, X. F.; Huggins, R. A.; Cui, Y. High-Performance Lithium Battery Anodes Using Silicon Nanowires. *Nat. Nanotechnol.* **2008**, *3*, 31–35.
5. Ryu, I.; Choi, J. W.; Cui, Y.; Nix, W. D. Size-Dependent Fracture of Si Nanowire Battery Anodes. *J. Mech. Phys. Solids* **2011**, *59*, 1717–1730.
6. Huggins, R.; Nix, W. Decrepitation Model for Capacity Loss During Cycling of Alloys in Rechargeable Electrochemical Systems. *Ionics* **2000**, *6*, 57–63.
7. Zhao, K. J.; Pharr, M.; Vlassak, J. J.; Suo, Z. G. Fracture of Electrodes in Lithium-Ion Batteries Caused by Fast Charging. *J. Appl. Phys.* **2010**, *108*, 073517.
8. Woodford, W. H.; Chiang, Y.-M.; Carter, W. C. "Electrochemical Shock" of Intercalation Electrodes: A Fracture Mechanics Analysis. *J. Electrochem. Soc.* **2010**, *157*, A1052–A1059.
9. Takamura, T.; Ohara, S.; Uehara, M.; Suzuki, J.; Sekine, K. A Vacuum Deposited Si Film Having a Li Extraction Capacity over 2000 Mah/G with a Long Cycle Life. *J. Power Sources* **2004**, *129*, 96–100.
10. Graetz, J.; Ahn, C. C.; Yazami, R.; Fultz, B. Nanocrystalline and Thin Film Germanium Electrodes with High Lithium Capacity and High Rate Capabilities. *J. Electrochem. Soc.* **2004**, *151*, A698–A702.
11. Magasinski, A.; Dixon, P.; Hertzberg, B.; Kvit, A.; Ayala, J.; Yushin, G. High-Performance Lithium-Ion Anodes Using a Hierarchical Bottom-up Approach. *Nat. Mater.* **2010**, *9*, 353–358.
12. Zhou, S.; Liu, X. H.; Wang, D. W. Si/$TiSi_2$ Heteronanostructures as High-Capacity Anode Material for Li Ion Batteries. *Nano Lett.* **2010**, *10*, 860–863.
13. Kasavajjula, U.; Wang, C. S.; Appleby, A. J. Nano- and Bulk-Silicon-Based Insertion Anodes for Lithium-Ion Secondary Cells. *J. Power Sources* **2007**, *163*, 1003–1039.
14. Zhang, W.-J. A Review of the Electrochemical Performance of Alloy Anodes for Lithium-Ion Batteries. *J. Power Sources* **2011**, *196*, 13–24.
15. Choi, H. S.; Lee, J. G.; Lee, H. Y.; Kim, S. W.; Park, C. R. Effects of Surrounding Confinements of Si Nanoparticles on Si-Based Anode Performance for Lithium Ion Batteries. *Electrochim. Acta* **2010**, *56*, 790–796.
16. Hu, L.; Wu, H.; Gao, Y.; Cao, A.; Li, H.; McDough, J.; Xie, X.; Zhou, M.; Cui, Y. Silicon−Carbon Nanotube Coaxial Sponge as Li-Ion Anodes with High Areal Capacity. *Adv. Energy Mater.* **2011**, *1*, 523–527.
17. Cui, L. F.; Yang, Y.; Hsu, C. M.; Cui, Y. Carbon−Silicon Core−Shell Nanowires as High Capacity Electrode for Lithium Ion Batteries. *Nano Lett.* **2009**, *9*, 3370–3374.
18. Cui, L.-F.; Hu, L.; Choi, J. W.; Cui, Y. Light-Weight Free-Standing Carbon Nanotube−Silicon Films for Anodes of Lithium Ion Batteries. *ACS Nano* **2010**, *4*, 3671–3678.
19. Choi, N.-S.; Yao, Y.; Cui, Y.; Cho, J. One Dimensional Si/Sn-Based Nanowires and Nanotubes for Lithium-Ion Energy Storage Materials. *J. Mater. Chem.* **2011**, *21*, 9825–9840.
20. Wen, C. J.; Huggins, R. A. Chemical Diffusion in Intermediate Phases in the Lithium-Silicon System. *J. Solid State Chem.* **1981**, *37*, 271–278.
21. Obrovac, M. N.; Christensen, L. Structural Changes in Silicon Anodes During Lithium Insertion/Extraction. *Electrochem. Solid-State Lett.* **2004**, *7*, A93–A96.
22. Hatchard, T. D.; Dahn, J. R. *In Situ* XRD and Electrochemical Study of the Reaction of Lithium with Amorphous Silicon. *J. Electrochem. Soc.* **2004**, *151*, A838–A842.
23. Liu, X. H.; Zhang, L. Q.; Zhong, L.; Liu, Y.; Zheng, H.; Wang, J. W.; Cho, J.-H.; Dayeh, S. A.; Picraux, S. T.; Sullivan, J. P.; *et al.* Ultrafast Electrochemical Lithiation of Individual Si Nanowire Anodes. *Nano Lett.* **2011**, *11*, 2251–2258.
24. Liu, X. H.; Zheng, H.; Zhong, L.; Huang, S.; Karki, K.; Zhang, L. Q.; Liu, Y.; Kushima, A.; Liang, W. T.; Wang, J. W.; *et al.* Anisotropic Swelling and Fracture of Silicon Nanowires During Lithiation. *Nano Lett.* **2011**, *11*, 3312–3318.
25. Lee, S. W.; McDowell, M. T.; Berla, L. A.; Nix, W. D.; Cui, Y. Fracture of Crystalline Silicon Nanopillars During Electrochemical Lithium Insertion. *Proc. Natl. Acad. Sci. U.S.A.* **2012**, *109*, 4080–4085.
26. Goldman, J. L.; Long, B. R.; Gewirth, A. A.; Nuzzo, R. G. Strain Anisotropies and Self-Limiting Capacities in Single-Crystalline 3d Silicon Microstructures: Models for High Energy Density Lithium-Ion Battery Anodes. *Adv. Funct. Mater.* **2011**, *21*, 2412–2422.
27. Lee, S. W.; McDowell, M. T.; Choi, J. W.; Cui, Y. Anomalous Shape Changes of Silicon Nanopillars by Electrochemical Lithiation. *Nano Lett.* **2011**, *11*, 3034–3039.
28. Wang, C.-M.; Li, X.; Wang, Z.; Xu, W.; Liu, J.; Gao, F.; Kovarik, L.; Zhang, J.-G.; Howe, J.; Burton, D. J.; *et al.* *In Situ* TEM Investigation of Congruent Phase Transition and Structural Evolution of Nanostructured Silicon/Carbon Anode for Lithium Ion Batteries. *Nano Lett.* **2012**, *12*, 1624–1632.
29. Ng, S. H.; Wang, J. Z.; Wexler, D.; Konstantinov, K.; Guo, Z. P.; Liu, H. K. Highly Reversible Lithium Storage in Spheroidal Carbon-Coated Silicon Nanocomposites as Anodes for Lithium-Ion Batteries. *Angew. Chem., Int. Ed.* **2006**, *45*, 6896–6899.
30. Huang, R.; Fan, X.; Shen, W. C.; Zhu, J. Carbon-Coated Silicon Nanowire Array Films for High-Performance Lithium-Ion Battery Anodes. *Appl. Phys. Lett.* **2009**, *95*, 133119.
31. Ghassemi, H.; Au, M.; Chen, N.; Heiden, P. A.; Yassar, R. S. *In Situ* Electrochemical Lithiation/Delithiation Observation

of Individual Amorphous Si Nanorods. *ACS Nano* **2011**, *5*, 7805–7811.
32. Liu, X. H.; Huang, J. Y. *In Situ* TEM Electrochemistry of Anode Materials in Lithium Ion Batteries. *Energy Environ. Sci.* **2011**, *4*, 3844–3860.
33. Liu, X. H.; Liu, Y.; Kushima, A.; Zhang, S.; Zhu, T.; Li, J.; Huang, J. Y. *In Situ* TEM Experiments of Electrochemical Lithiation and Delithiation of Individual Nanostructures. *Adv. Energy Mater.* **2012**, *2*, 722–741.
34. Liu, Y.; Zheng, H.; Liu, X. H.; Huang, S.; Zhu, T.; Wang, J.; Kushima, A.; Hudak, N. S.; Huang, X.; Zhang, S.; *et al.* Lithiation-Induced Embrittlement of Multiwalled Carbon Nanotubes. *ACS Nano* **2011**, *5*, 7245–7253.
35. Hertzberg, B.; Alexeev, A.; Yushin, G. Deformations in Si-Li Anodes Upon Electrochemical Alloying in Nano-Confined Space. *J. Am. Chem. Soc.* **2010**, *132*, 8548–8549.
36. Sethuraman, V. A.; Chon, M. J.; Shimshak, M.; Srinivasan, V.; Guduru, P. R. *In Situ* Measurements of Stress Evolution in Silicon Thin Films During Electrochemical Lithiation and Delithiation. *J. Power Sources* **2010**, *195*, 5062–5066.
37. Zhao, K. J.; Pharr, M.; Vlassak, J. J.; Suo, Z. G. Inelastic Hosts as Electrodes for High-Capacity Lithium-Ion Batteries. *J. Appl. Phys.* **2011**, *109*, 016110.
38. Liu, X. H.; Wang, J. W.; Liu, Y.; Zheng, H.; Kushima, A.; Huang, S.; Zhu, T.; Mao, S. X.; Li, J.; Zhang, S.; *et al.* *In Situ* Transmission Electron Microscopy of Electrochemical Lithiation, Delithiation and Deformation of Individual Graphene Nanoribbons. *Carbon* **2012**, *50*, 3836–3844.
39. Zhao, K.; Pharr, M.; Cai, S.; Vlassak, J. J.; Suo, Z. Large Plastic Deformation in High-Capacity Lithium-Ion Batteries Caused by Charge and Discharge. *J. Am. Ceram. Soc.* **2011**, *94*, S226–S235.
40. Demczyk, B. G.; Wang, Y. M.; Cumings, J.; Hetman, M.; Han, W.; Zettl, A.; Ritchie, R. O. Direct Mechanical Measurement of the Tensile Strength and Elastic Modulus of Multiwalled Carbon Nanotubes. *Mater. Sci. Eng., A* **2002**, *334*, 173–178.
41. Hertzberg, B.; Benson, J.; Yushin, G. *Ex-Situ* Depth-Sensing Indentation Measurements of Electrochemically Produced Si−Li Alloy Films. *Electrochem. Commun.* **2011**, *13*, 818–821.
42. Hill, R. *The Mathematical Theory of Plasticity*; Oxford University Press: Oxford, 1950.
43. Liu, X. H.; Huang, S.; Picraux, S. T.; Li, J.; Zhu, T.; Huang, J. Y. Reversible Nanopore Formation in Ge Nanowires During Lithiation−Delithiation Cycling: An *In Situ* Transmission Electron Microscopy Study. *Nano Lett.* **2011**, *11*, 3991–3997.